Impurity study in the dimensionless and dimensional isotope identity experiment between JET Deuterium and Tritium L-mode plasmas

Downloaded from: https://research.chalmers.se, 2026-09-14 08:38 UTC

Citation for the original published paper (version of record):
Czarnecka, A., Joffrin, E., Wischmeier, M. et al (2025). Impurity study in the dimensionless and dimensional isotope identity experiment between JET
Deuterium and Tritium L-mode plasmas. Nuclear Fusion, 65(1).
http://dx.doi.org/10.1088/1741-4326/ad9758

N.B. When citing this work, cite the original published paper.

research.chalmers.se offers the possibility of retrieving research publications produced at Chalmers University of Technology. It covers all kind of research output: articles, dissertations, conference papers, reports etc. since 2004. research.chalmers.se is administrated and maintained by Chalmers Library

(article starts on next page)

nuclear fusion
IAEA

PAPER • OPEN ACCESS

Impurity study in the dimensionless and dimensional isotope identity experiment between JET Deuterium and Tritium L-mode plasmas

To cite this article: A. Chomiczewska *et al* 2025 *Nucl. Fusion* **65** 016045

View the article online for updates and enhancements.

You may also like

- Impurity transport driven by kinetic ballooning mode in the strong gradient pedestal of tokamak plasmas
Shanni Huang, Weixin Guo and Lu Wang
- Non-linear dependence of ion heat flux on plasma density at the L–H transition of JET NBI-heated deuterium–tritium plasmas
P. Vincenzi, E.R. Solano, E. Delabie et al.
- The impact of helium on plasma-driven hydrogen permeation and implications for direct internal recycling in the fusion fuel cycle
Chao Li, J. Douglas Way, Thomas F. Fuerst et al.

This content was downloaded from IP address 129.16.31.207 on 10/06/2026 at 13:26

OPEN ACCESS
IOP Publishing | International Atomic Energy Agency
Nuclear Fusion
Nucl. Fusion **65** (2025) 016045 (14pp)
https://doi.org/10.1088/1741-4326/ad9758

Impurity study in the dimensionless and dimensional isotope identity experiment between JET Deuterium and Tritium L-mode plasmas

A. Chomiczewska[1,*], T. Tala[2], W. Gromelski[1], I. Ivanova-Stanik[1], E. Kowalska-Strzęciwilk[1], N. Wendler[1], I.S. Carvalho[3], P. Carvalho[4], I. Coffey[4], A. Kirjasuo[2], M. Lennholm[4], S. Menmuir[4], G. Pucella[5], A. Salmi[2], B. Thomas[4], JET contributors[a] and the EUROfusion Tokamak Exploitation Team[b]

EUROfusion Consortium, JET, Culham Science Centre, Abingdon OX14 3DB, United Kingdom of Great Britain and Northern Ireland

[1] Institute of Plasma Physics and Laser Microfusion, Warsaw, Poland
[2] VTT, PO Box 1000, FI-02044 VTT Espoo, Finland
[3] ITER Organization, Route de Vinon sur Verdon, 13115 St Paul Lez Durance, France
[4] UKAEA, CCFE, Culham Science Centre, Abingdon, Oxon OX14 3DB, United Kingdom of Great Britain and Northern Ireland
[5] Fusion and Nuclear Safety Department, ENEA, Frascati, Italy

E-mail: agata.chomiczewska@ifpilm.pl

Received 21 May 2024, revised 9 November 2024
Accepted for publication 26 November 2024
Published 9 December 2024

Abstract

The behaviour of impurities in fusion plasmas is of crucial importance for achieving sustained fusion reactions, and understanding similarities and differences between Deuterium (D) and Tritium (T) plasmas is needed to assess potential changes from DD to DT in ITER and future reactors. The first dimensionless and dimensional isotope identity experiments between Deuterium (D) and Tritium (T) L-mode plasmas were conducted at the JET W/Be wall. In the first approach, the discharges with matched $\rho*$, $\nu*$, β_n, q, and T_e/T_i were compared to emphasize direct isotope effects, while in the dimensional approach engineering parameters such as toroidal magnetic field B_T, plasma current I_p, plasma electron density and NBI power P_{NBI} were matched. The dimensionless isotope scaling showed an improvement in global confinement and local transport in T plasmas in comparison to the matched D one (Cordey *et al* 1999 *Nucl. Fusion* **39** 301). Detailed impurity analyses using VUV, visible spectroscopy, SXR cameras, and bolometry revealed that T plasmas exhibited higher radiation and impurity

[a] See Maggi *et al* 2024 (https://doi.org/10.1088/1741-4326/ad3e16) for JET Contributors.
[b] See Joffrin *et al* 2024 (https://doi.org/10.1088/1741-4326/ad2be4) for the EUROfusion Tokamak Exploitation Team.
[*] Author to whom any correspondence should be addressed.

Original content from this work may be used under the terms of the Creative Commons Attribution 4.0 licence. Any further distribution of this work must maintain attribution to the author(s) and the title of the work, journal citation and DOI.

content, particularly Ni and W, compared to D plasmas. Understanding the origin of the increased impurity content is addressed in this paper. The dimensionless experiments showed differences in impurity transport. The Be source behaviour varied: D plasmas had higher Be influx in the dimensionless approach due to lower electron density and enhanced sputtering (Saibene *et al* 1999 *Nucl. Fusion* **39** 1133), while T plasmas showed a higher Be source in the dimensional experiments, highlighting isotope mass effects. W in the divertor region was not sputtered by hydrogen isotopes. W in the divertor region was not sputtered by hydrogen isotopes. In the dimensionless experiments, W sputtering was primarily influenced by Ni in T plasmas and by Be in D plasmas. However, in the dimensional approach, Be played a more significant role in W sputtering within T plasmas. MHD instabilities, including ST oscillations, were present in all cases other ones were correlated with NBI power levels; higher NBI power led to elevated levels of Be, Ni, and W impurities. The comprehensive comparison underscores the necessity of accounting for isotope mass effects in predictive modelling and optimization of plasma performance in fusion reactors.

Keywords: fusion, tokamak, impurities, tritium plasmas, H isotopes

(Some figures may appear in colour only in the online journal)

1. Introduction

The isotope mass (A) scaling of the global energy confinement time τ_{E} and the thermal energy confinement time $\tau_{\mathrm{E,th}}$ can be significantly different depending on the plasma regimes. Conducted research on the JET tokamak with the carbon wall (C-wall) showed different scaling of confinement for ELM-free and ELMy H-mode plasmas [1] or high-density H-mode [2]. For type I ELM H-mode plasmas confinement scaling improve by changing the C-wall [1] to the JET ITER-like wall (ILW) with beryllium (Be) limiter and tungsten (W) divertor [3]. In the JET-ILW tests were also done for NBI, L-mode [3] and a weak isotope dependence was observed. The isotope mass scaling in L-mode and H-mode conditions was significantly different. Understanding the effect of A on heat and particle transport is still incomplete and most of the existing studies at JET-ILW are based on the comparison of hydrogen (H) and deuterium (D) plasmas [3, 4]. However, future fusion power plants and experimental reactors, such as ITER, will operate with deuterium-tritium (D-T) plasmas. In the past only on two devices in the world, TFTR [5, 6], and JET C-wall [1] isotope scaling of confinement between D and T plasmas was studied. Recent JET T and D-T campaigns were a unique opportunity to study core confinement in D and T plasmas in reactor-relevant plasma conditions [7, 8]. It was found, that due to the lack of a pedestal, the isotope scaling in the plasma core is significantly different in the L-mode [7] in comparison to H-mode [8] plasmas. As it was reported in [9] the pedestal density is isotope dependent. The dimensionless isotope mass scaling experiment between D and T plasmas showed the improvement in global confinement and local transport in tritium L-mode plasmas was found in comparison to deuterium one [7]. However, despite the better plasma confinement also higher impurity radiation was observed. Understanding the origin of observed increased intrinsic impurity content in T plasma is addressed in this paper. As D and T isotopes differ by 50% in mass, impurities may experience different transport properties depending on the predominant isotopic species present in the plasma. This can affect impurity diffusion, convection, and drift processes within the plasma [10–14]. Changes in the isotopic composition of hydrogen can impact the overall plasma composition, including impurity concentrations and distributions. Isotopic differences can influence the mechanisms of plasma-surface interactions, affecting impurity sources. Consequently, different hydrogen isotopes can influence impurity radiation properties differently by altering plasma temperature, density, and confinement. Changes in plasma conditions due to isotope effects may affect impurity excitation, ionization, and radiative cooling rates. Understanding the hydrogen isotope effect on intrinsic impurities in tokamak plasmas is crucial for plasma control, impurity mitigation, and the optimization of fusion performance. This study is focused on experimental data analysis and numerical simulations with special emphasis on the impurity behaviour in the dimensionless and also in dimensional isotope identity experiment to assess for the first time the effect of plasma isotopes, in JET-ILW D and T L-mode plasmas. These approaches are crucial for understanding the fundamental differences and similarities in plasma behaviour when switching between different isotopes. The dimensionless approach is essential for theoretical and model validation, ensuring that plasma behaviour can be understood and predicted across different scenarios. This approach provides insights that can be extrapolated to different machines including future reactors like ITER, where different isotopes will be used. It helps in understanding how results from current experiments might scale to larger or more complex systems. The dimensional approach is crucial for practical applications. It allows for a direct comparison of how D and T plasmas behave under the same machine settings. This is essential for planning and optimizing actual fusion reactor operations. It provides data on how a reactor might need to be adjusted when switching from D to T, such as changes in heating power, fuelling, or impurity management. Both approaches

together provide a comprehensive understanding of isotope effects in fusion plasmas. The work aims to determine whether the differences in impurity behaviour can be explained by differences in the plasma properties, impurity source and transport due to the isotope effect. Detailed impurity analyses are presented for both approaches to disentangle the direct and indirect impact of different isotope masses. In section 2, both experimental and numerical modelling results are discussed for the dimensionless isotope identity experiment. In section 3, the dimensional isotope identity experiment and the results are described. Finally, conclusions are given in section 4.

2. The dimensionless isotope identity experiment

The experimental and theoretical analyses were focused on L-mode discharges performed in D and T plasmas with matched dimensionless quantities of normalised Larmor radius ρ^*, normalised collisionality ν^*, normalized beta β_N, and safety factor q, in the confinement plasma region, which are defined by following equations from [7]

$$\rho_i^* = 4.57 \times 10^{-3} \sqrt{AT_i}/(aB_t) \quad (1)$$

$$\nu^* = 17 n_e e^2 R_0^{2.5} Z_{eff} q_{95} / 12\pi^{1.5} \varepsilon_0^2 T_e^2 a^{1.5} \quad (2)$$

$$\beta_N = \beta a B_t / I_p \quad (3)$$

$$\beta = 2\mu_0 (p_e + p_i)/B_t^2 \quad (4)$$

$$q = aB_t / R_0 B_p \quad (5)$$

where A is mass number, T_i, T_e—ion and electron temperature, a and R_0—minor and major radius, B_t and B_p—toroidal and poloidal magnetic field, I_p—plasma current, n_e—electron density, e—elementary charge, Z_{eff}—effective charge, q_{95}—safety factor, ε_0—permittivity, μ_0—permeability, p_e and p_i—electron and ion pressure. The methodology relies on maintaining invariance to changes in dimensional plasma parameters, such as density and temperature, while ensuring that the dimensionless plasma parameters remain conserved [3, 15]. By matching these dimensionless parameters, the goal is to achieve similarity in the turbulence and transport processes between D and T plasmas. Any observed differences in transport or confinement can be directly attributed to the isotope effects. The relations between the dimensionless quantities and the dimensionless energy confinement time $\Omega_{i\,\tau E,th}$ can be written according to the equation (6) as in [3, 7, 15]

$$\Omega_i\, \tau_{E,th} \sim \left(\rho^{*-\alpha_\rho}\, \beta^{-\alpha_\beta}\, \nu^{*-\alpha\nu_\nu}\, q^{-\alpha q}\, A^{-\alpha A} \ldots\right). \quad (6)$$

To keep ρ^*, ν^*, β_n, q and T_e/T_i profiles fixed when also varying the isotope mass A, the toroidal magnetic field, plasma current, temperature and density must scale, respectively, as B_t and $I_p \sim A^{3/4}$, $T \sim A^{1/2}$, and $n \sim A$ [16]. To achieve the required temperature and density profiles to match the dimensionless quantities in T and D plasmas, NBI power and gas puff had to be adjusted. The time evolution of main plasma parameters for the I_p and B_t, for the auxiliary NBI heating power (P_{NBI}), major gas puff rate, line average electron density ($n_{e,lad}$), central electron temperature ($T_e(0)$), stored diamagnetic plasma energy (W_{dia}) and for the total radiated power (P_{rad}) for D shot #96092 and T shot #100143 are illustrated in figure 1. A dimensionless isotope mass scaling pair, as it is listed in table 1, was executed at $B_t = 2.20$ T and $I_p = 1.79$ MA in D plasma and at $B_t = 2.98$ T and $I_p = 2.44$ MA in T plasma with the NBI power level 0.83 MW and 1.45 MW, respectively. The gas puff modulation technique was exploited as the additional tool to quantify the electron particle transport as presented in [7]. For the time intervals at 13–14 s for the T pulse and 17–18 s for the D pulse, indicated by the two vertical black lines in figure 1, a good dimensionless D versus T match was achieved. Kinetic profiles and matched dimensionless parameters are presented in figure 2. The same time of interest has been taken for further impurity transport analysis. In the experiments, the low triangularity, X-point plasmas configuration with the outer divertor strike point on the vertical target was used (see figure 3). The vertical (tile 7) and horizontal tiles (tile 4, 6) are made of tungsten (W) coated Carbon Facing Component (CFC). Both the divertor semi-horizontal tile (tile 5) and the main chamber NBI shine-through protection plates made of bulk W are the sources of W impurity in JET-ILW plasmas. Tritium was injected into the machine vacuum chamber through dedicated tritium introduction modules (TIMs) [17]. The subdivertor optical Penning gauge discharge spectroscopy [18] was used to measure the hydrogen-/deuterium/tritium (H/D/T) isotope ratio. The technical details of the method are described in Vartanian *et al* [18]. In T pulse #100143, residual hydrogen and deuterium in the vessel walls, due to absorption and outgassing, resulted in a measured T concentration of 98 %. For D shot #96092, a deuterium concentration of 99% was measured.

2.1. Plasma radiation and intrinsic impurity analysis of the dimensionless isotope identity experiment

The bolometry diagnostics [19] was used to measure the total radiated power (P_{rad}) and the radiated power density. The bolometry data measured along the orange lines of sight illustrated in figure 3 have been used for the tomographic reconstructions. The 2D radiation power density map is presented in figure 4. It can be seen that radiated power density, both in the central and divertor plasmas is larger in T discharge compared to D one.

It is to be noted that, unlike D discharges, in the T discharges described in this paper, neon (Ne) at a continuous gas rate of 1.2×10^{20} el/s during an extended range of the discharge was injected into the plasmas to improve the quality of Charge Exchange (CX) data for ion temperature and rotation measurements. This improvement is achieved through increased signal intensity, the provision of clear and distinct spectral lines, and a reduction in background interference. Additionally, Ne injection enables more localized measurements and aids in the calibration of diagnostic systems. Collectively, these factors contribute to more precise and reliable plasma diagnostics. Experimental reconstruction of 1-D

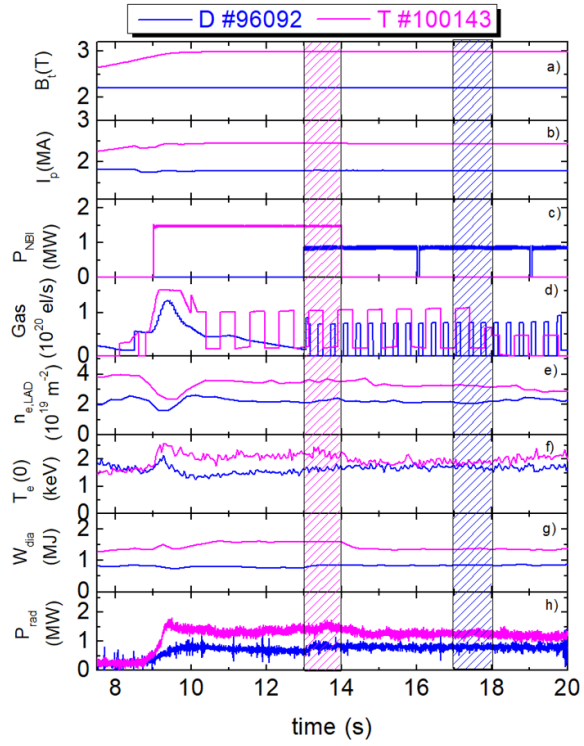

Figure 1. Time evolution of (*a*) the magnetic field B_t, (*b*) plasma current I_p, (*c*) the NBI heating power P_{NBI}, (*d*) major gas injection level, (*e*) the line average electron density n_{lad}, (*f*) the central electron temperature $T_e(0)$, (*g*) the diamagnetic energy W_{dia}, and (*h*) the total radiated power $P_{rad,}$ for D (blue, #96092) and T (magenta, #100143) discharges. The two vertical black bars indicate the times of interest in these pulses, at 13–14 s for the T pulse and 17–18 s for the D pulse.

Table 1. The comparison of toroidal magnetic field B_t, plasma current I_p, NBI heating power (P_{NBI}), and ohmic heating (P_{oh}), for the D (#96092) and T (#100143) dimensionless isotope mass scaling pair.

	D:#96092	T: #100143
B_t (T)	2.20	2.98
I_p (MA)	1.79	2.44
P_{NBI} (MW)	0.83	1.45
P_{OH} (MW)	1.26	1.47

profiles of the radiated power density presented in figure 5, derived from the 2D plots of figure 4 shows higher radiation peaking for the T pulse.

At JET-ILW the main contributors to the radiated power P_{rad} are high-Z (W) and mid-Z (e.g. nickel (Ni), copper (Cu), iron (Fe)) plasma impurities. During the performed experiments, a composition of plasma impurities was monitored using passive VUV spectroscopy diagnostic, known locally as KT2. The JET VUV SPRED survey spectrometer [20], with the line-of-sight presented in figure 3 (green horizontal line) measures spectra in the 100–1100 Å wavelength range, with a spectral resolution of ∼5 Å. In this spectral region, all mid-Z metallic impurity elements occurring in the JET plasmas are registered. The origin of such impurities is described in detail in [21]. Also, the high number of W transitions fall in this spectral region therefore, the W unresolved transition arrays (UTAs) are observed between wavelengths of ∼140–260 Å. The UTA observed by KT2 diagnostic is related to the W-ions W^{14+}–W^{35+} [21]. However, to avoid other elements interfering with lines, alternative measurements of the W spectrum, proposed in [21], were used. Denoted in the text I_W was measured by an integration of the VUV spectrum between wavelengths 176 and 201 Å. The background determined at a wavelength of 142 Å was subtracted from the integrated area. The mid-Z element concentrations were determined based on the method described in detail in [22]. The quantitative measurement of W concentration was not possible due to a lack of working XUV, and SXR diagnostics which were routinely used in JET-ILW before the use of T fuel [23–26].

Figure 6 shows the comparison of P_{rad}, I_w and Ni concentration (c_Ni) for the time intervals with matched dimensionless quantities between D and T plasmas. It was found that both the radiated power, I_w and c_Ni were around 2 times higher in the T discharge with respect to the D one. Concentrations of Cu and Fe were found to be negligible. The JET-ILW is the fusion device operating with the Be limiter that protects the inner and outer first wall. To indicate the behaviour of the Be source in the main chamber, data from the visible spectroscopy (KSRA survey spectrometer) with the line of sight presented in figure 3(*a*), were analysed. Figure 7 shows the photon flux of the Be II line measured at wavelength 467 nm. The minima and maxima observed in the signals are related to the gas puff

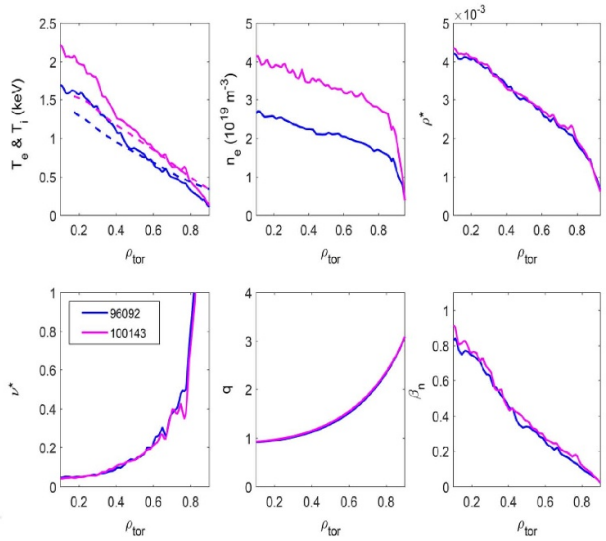

Figure 2. Comparison of electron T_e (solid curve) and ion temperatures T_i (dashed curve), electron densities and dimensionless quantities ρ^*, ν^*, q, β_n in D (#96092) and T (#100143) plasmas as a function of the normalized radius and averaged in time between t = 13–14 s for the T pulse and t = 17–18 s for the D pulse.

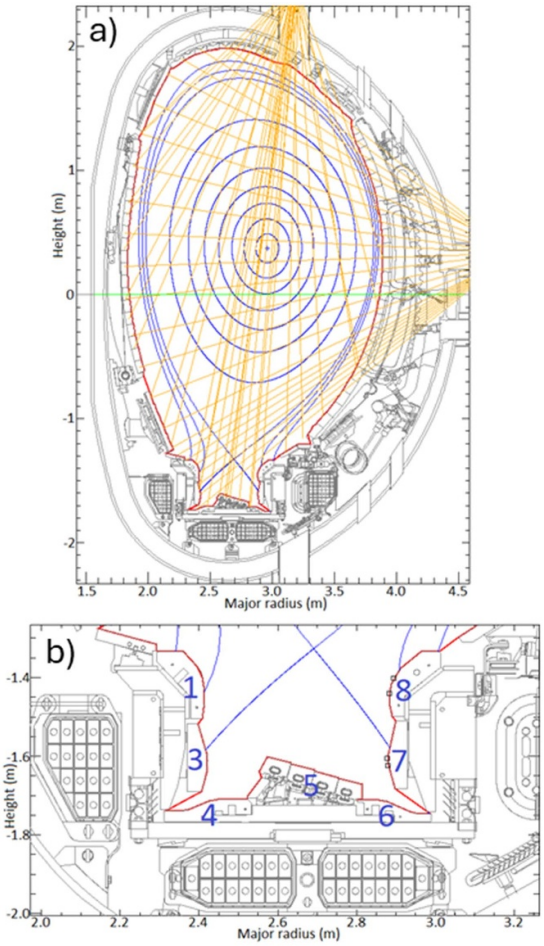

Figure 3. (*a*) Poloidal cross-section with the plasma configurations with the lines of sight of JET VUV, visible spectrometers (green horizontal line) and bolometry diagnostics (orange lines) on JET tokamak. (*b*) Magnetic configuration in the divertor with the inner and outer strike points on the vertical targets. The outer Langmuir probes used in the analysis are shown in black squares.

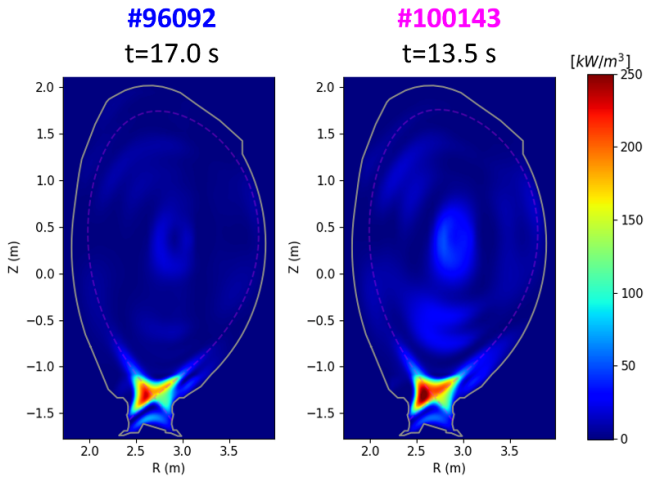

Figure 4. Tomographic reconstruction of the radiated power density in pulse #96092 at $t = 17$ s for the D plasmas and in pulse #100143 at $t = 13.5$ s for the T plasmas.

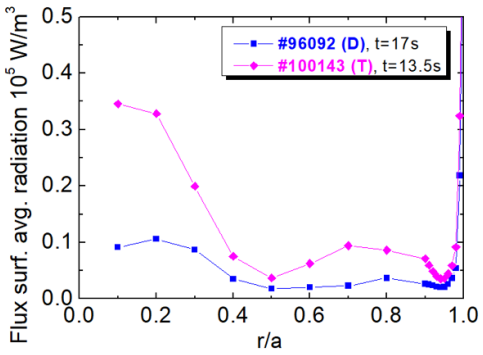

Figure 5. The flux-surface averaged profiles of the radiated density derived from the bolometry diagnostic as a function of the normalised radius for D discharge #96092 at t = 17 s and for T discharge #100143 at t = 13.5 s.

modulation. It can be seen that the Be source is higher in the D pulse in comparison to T. As was observed in [27] Be source at JET-ILW increased with the isotope mass. The temperatures measured by the protection cameras looked at the inner, outer, and top of Be limiters were similar in both discharges and reached 600 °C. However, in the dimensionless experiment, the influence of different n_e on Be source is observed. As shown in figure 2, T pulse #100143 has 50% higher electron density in comparison to D pulse #96092. For higher n_e decrease in Be source is observed. Observations agree with the analysis presented in [28, 29], where for a specific magnetic configuration and limited density range the Be effective sputtering yield decreases with n_e. The reduction of the Be source in T plasmas can be also explained by the reduction in the heat load on the Be-limiter due to Ne injection. Thus, in dimensionless experiments, competition between several processes dictates the final shape of the emission. Different behaviour of high-Z and mid-Z impurities between T and D plasmas is related to the isotope effect.

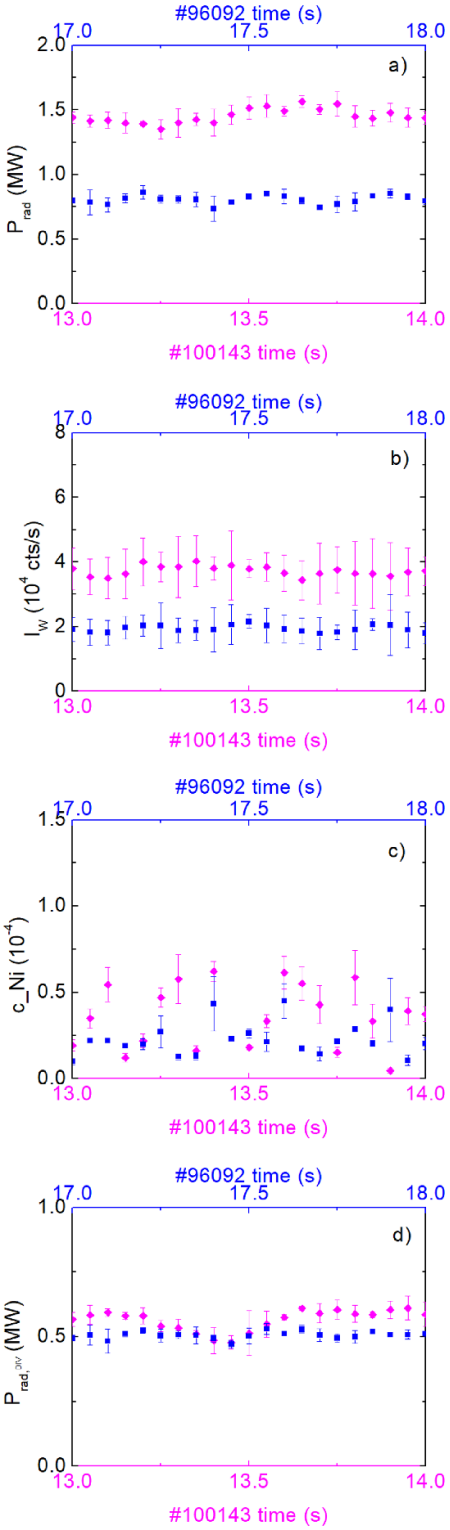

Figure 6. (*a*) The total radiated power, (*b*) I_W, (*c*) cNi and (*d*) divertor radiated power P_{rad},^{DIV} in the time of interest for the T pulse #100143 ($t = 13$–14 s) and for the D pulse #96092 ($t = 17$–18 s).

The presence of Be, Ne and Ni ions in the divertor plasmas can affect W sputtering. Divertor tiles are exposed to impurity particle fluxes from the main chamber, leading to W sputtering, erosion, and deposition processes [30, 31]. The divertor radiated power (P_{rad},^{DIV}) presented in figure 6(*d*), derived

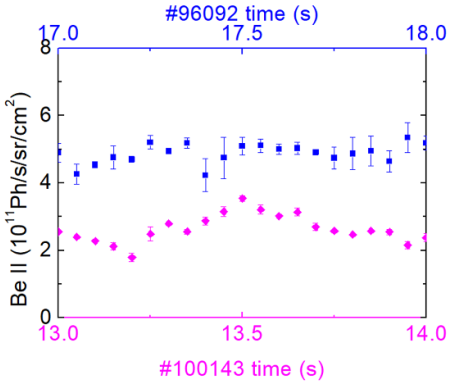

Figure 7. The photon flux of the Be II line at 467 nm, measured at the outer poloidal limiter for the T pulse #100143 (t = 13–14 s) and for the D pulse #96092 (t = 17–18 s).

as the difference between the total and the core radiation, shows slightly higher radiation in T plasmas. Unfortunately, the quantitative data of the W divertor source, for vertical target configurations, used in these experiments, are unavailable. This is because the calculation of the W flux based on the combination of a visible spectrometer and photodiodes is feasible provided that the strike point position is located on the semi-horizontal bulk-W target plates known as tile 5. In other cases, the spectra are dominated by the noise impeding trustworthy calculations. However, the analysis of the divertor plate temperature $T_{e,}^{PLATE}$, the plasma ion flux flowing to the target and the electron pressure can provide ideas about possible W production. Such parameters were measured by the Langmuir probes (LPs) located in front of the outer vertical target, as illustrated in figure 3(*b*). In figure 8, a comparison of measured T_e^{PLATE}, the surface flux density, the ion saturation current, which represents the plasma ion flux flowing to the target, and the electron pressure are presented, for D and T discharges as a function of the distance along the target from the separatrix. It can be seen that $T_{e,}^{PLATE}$ is higher in D plasmas. In this comparison, all the other parameters are higher for T plasmas. However, both in D and T plasmas the plate temperature is lower than $T_{e,}^{PLATE} < 40$ eV, and according to [27, 32], in L-mode plasmas, W physical sputtering from the divertor is expected to be dominated by intrinsic impurity ions and not by hydrogen isotopes, for which higher temperatures $T_{e,}^{PLATE} > 70$ eV is needed. As it is also shown in [29], in L-mode plasmas, measured W sputtering yield and energy threshold are comparable for different hydrogen isotopes. W sputtering in T due to the higher isotope mass was only observed on JET in H-modes intra-ELMs, at high impinging ion energies [27, 32].

2.2. Modelling with the COREDIV code

The dimensionless isotope identity pair was simulated using the COREDIV code which couples self-consistently the plasma core with the scrape-off-layer (SOL). A full description of the code is given in [33, 34]. For given the experimentally measured plasma volume average electron density,

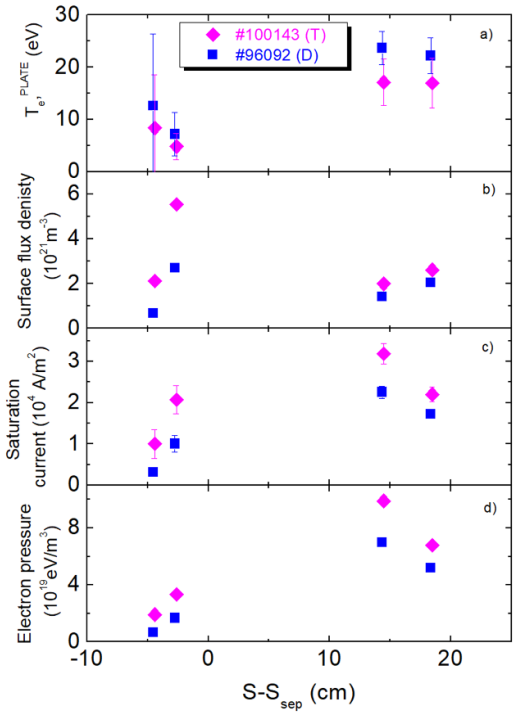

Figure 8. (*a*) The divertor plate electron temperature, (*b*) the surface flux density, (*c*) the saturation current and (*d*) the electron pressure measured by the Langmuir probes, as a function of distance along the vertical target from the separatrix for the T pulse #100143 averaged over time t = 13–14 s and for the D pulse #96092 averaged over time t = 17–18 s.

the toroidal magnetic field, input heating power, and radial transport coefficients in SOL ($D_{SOL} = 0.15$ m^2 s^{-1}), 1D radial transport equations were solved for impurity ions, bulk plasma ions and the electron and ion temperatures in core and 2D in SOL plasmas. Atomic processes such as ionization, recombination, excitation, and charge exchange have been included. In the COREDIV, the electron and ion energy fluxes are defined by the local transport model proposed in [35], which reproduces a prescribed energy confinement law. The radial impurity transport equation has a simple analytical form:

$$\frac{\partial n_{Z,j}}{\partial t} + \frac{1}{rg_1}\frac{\partial}{\mathrm{d}r}\left(rg_2\Gamma z,j\right) = S^n_{Z,j} \tag{7}$$

where $n_{Z,j}$ is the particle density of the impurity with atomic number Z in ion stage j, r is radial coordinate, g_1 and g_2 are matric coefficients, $\Gamma_{Z,j}$ represents impurity flux. $S^n_{Z,j}$ is a source term representing the production or loss of the impurity ion. The impurity flux $\Gamma_{Z,j}$ is defined as:

$$\Gamma z,j = \left(-D_{\mathrm{imp}}\frac{\mathrm{d}n_{Z,j}}{\partial r} + V_{\mathrm{imp}}n_{Z,j}\right) \tag{8}$$

where D_{imp} is the impurity diffusion coefficient and V_{imp} is the flux averaged impurity convection velocity. The ratio V_{imp}/D_{imp} is a dimensionless quantity that characterizes the relative importance of convective versus diffusive transport of impurities in the plasma. This ratio indicates the direction and strength of the impurity transport. If is positive and

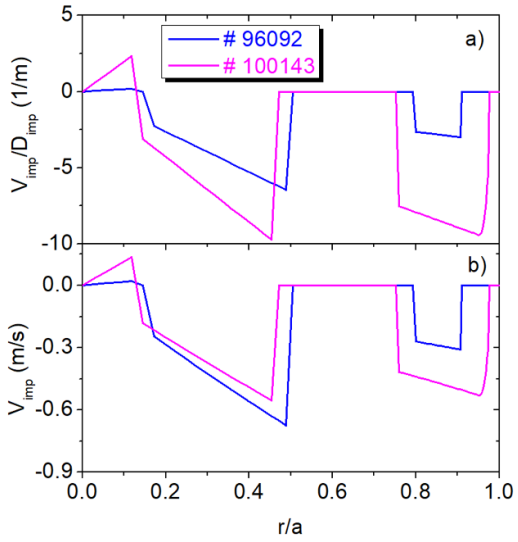

Figure 9. Comparison of the optimised (*a*) the impurity pinch velocity V_{imp}/D_{imp} and (*b*) the impurity convection coefficient V_{imp} in D and T plasma.

large, convective transport dominates and impurities are likely to be transported outwards. If it is negative, impurities are more likely to accumulate in the plasma core. Transport was assumed the same for all intrinsic impurities and all their ionization stages. Due to the unavailability of essential experimental data (for example the W concentration along the plasma radius), the impurity pinch velocity and the impurity convection coefficient were assumed different in D and T plasmas as presented in figure 9, to numerically reconstruct the experimental radiation density profile. The change in the core impurity content was also attributed to changes in the impurity transport between D and T due to changes in n_e and T_e.

For the D pulse, three impurities were considered, Be, W and Ni. In the T pulse additionally, Ne was also included. The Ni fluxes (1×10^{18} p s^{-1} and 1.4×10^{18} p s^{-1}, for the D and T pulse, respectively) and Ne flux (6×10^{18} p s^{-1} in the T pulse), given as a code input, were adjusted to reproduce the experimentally determined concentrations. In the lack of experimental data on the absolute Be fluxes, its input values (2.5 and 0.35×10^{20} p s^{-1} for the D and T pulse, respectively) were set arbitrarily to match Z_{eff}, W concentration and bolometric data. It was also considered that the experimental background level of the Be II line is higher for the D pulse than for the T pulse (see figure 7). Changes in the input Be fluxes resulted in changes in the radiated power density profile due to modifications of the W sputtering caused by Be ions. The W flux was self-consistently computed from sputtering at divertor targets by all ions. For the simulations of the D pulse #96092 and T pulses #100143, the times t = 17 s and t = 13.5 s were selected, respectively. In figure 10 the experimental electron temperature (T_e) and density (n_e) profiles from High-Resolution Thomson Scattering diagnostic (HRTS) and ion temperature (T_i) from Charge eXchange Recombination Spectroscopy

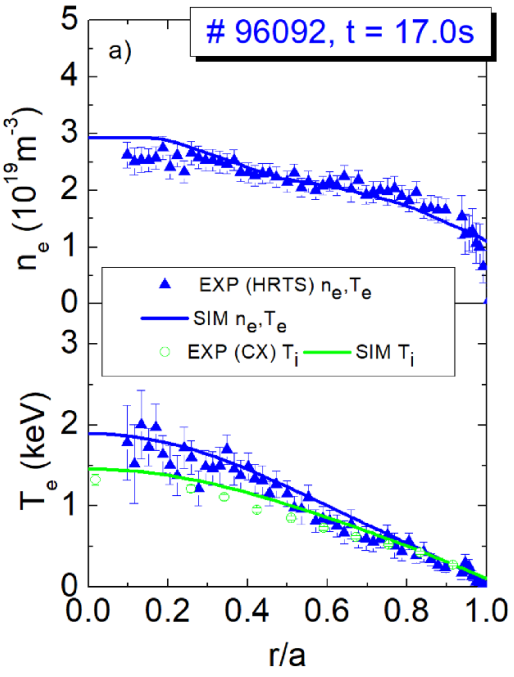

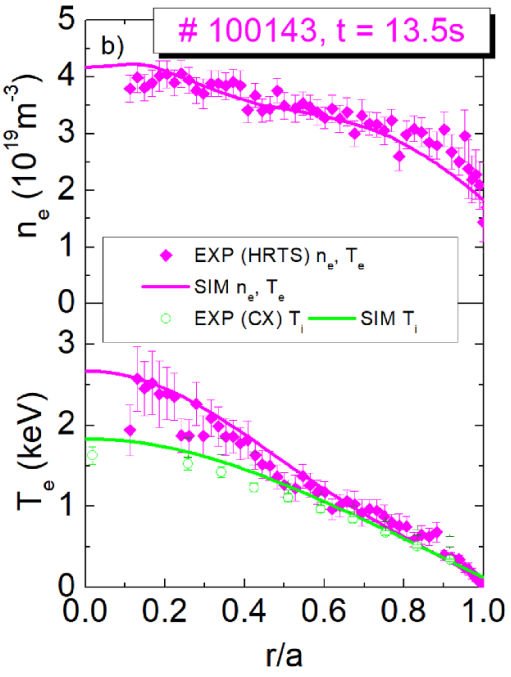

Figure 10. Experimental electron density (n_e) and temperature (T_e) profiles, for (*a*) D pulses #96092 (blue points) at $t = 17$ s, and (*b*) T pulse #100143 (magenta points) at 13.5 s and the corresponding COREDIV computed n_e, T_e, (black lines) and T_i profiles (red lines).

(CXRS) are compared with the numerical results. Within the uncertainties of the measurements, a good agreement between the experimental and simulated kinetic profiles was achieved.

In figure 11, a comparison of numerically reconstructed radiation density profiles are shown together with the experimental values, for the times of interest in the D and T

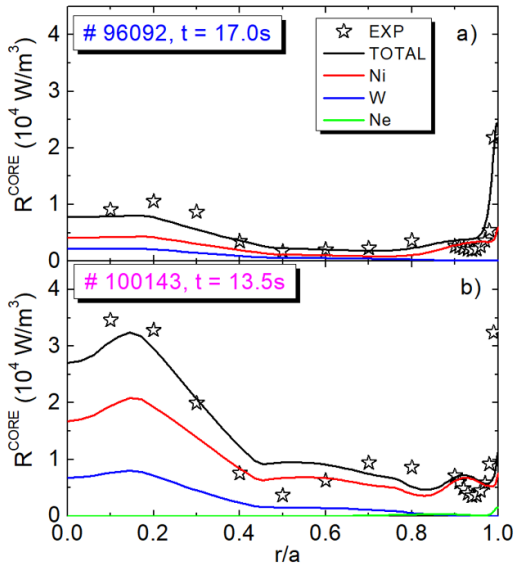

Figure 11. The COREDIV total (black line), nickel (red line), tungsten (blue line) and neon (green line), radiated power density profiles for (*a*) the D pulse at t = 17 s and (*b*) T pulse at t = 13.5 s. The stars correspond to the experimental points from the plots of figure 5.

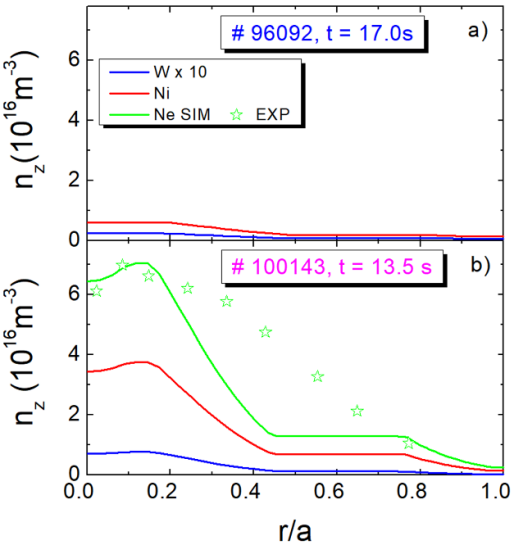

Figure 12. The COREDIV nickel (red line), tungsten (blue line) and neon (green line), density profiles for (*a*) the D pulse at t = 17 s and (*b*) the T pulse at t = 13.5 s. The stars correspond to experimental Ne density profiles determined from the CX diagnostic.

pulses considered. Additionally, the simulated Ni, W, and Ne radiation densities profiles are included. Simulations showed that the Ni radiation in the core plasmas is more than 50% of the core radiated power. Ne does not influence the plasma radiation in the confined region. In the whole normalized plasma radii, the higher Ni and W radiation are observed in T plasmas in which also stronger impurity peaking in the central region, r/a < 0.3, is observed. However, looking at the impurity densities presented in figure 12, it is possible to see that despite higher values for W and Ni densities in T plasmas in comparison to the D one, Ne density in the core of T plasmas is the highest. However, the Ne density value is very small in comparison to n_e and we can ignore it as one factor making a difference between D and T plasma in the core region. Higher impurity densities in T plasmas result from stronger impurity pinch in T plasma and the inward convective velocity in the edge region. A good agreement between theoretical and experimental central values of Ne density was obtained. The difference in Ne density values between experimental and simulated data in the range r/a = 0.3–0.7 in figure 12 is related to different transport for different impurities. Ne transport is different in the experiment than assumed in the simulation. This discrepancy may slightly impact W sputtering estimates. Nevertheless, this would have no impact on the conclusions. It must be noted that Ne flux at the plasma edge was adjusted to reproduce the experimentally determined average concentrations and higher Ne flux would also require a higher average Ne concentration. In the simplified slab geometry used in the COREDIV code [33], the simulated divertor plate electron temperature (T_e^{PLATE}), at the strike point $S - S_{sep} = 0$, is 11 eV and 6.25 eV for D and T plasmas, respectively, whereas, ion density on the divertor plate is 5.05×10^{19} m^{-3} in the case of D pulse and two times higher value 10.5×10^{19} m^{-3} in T discharge. Simulations are consistent with the LP measurements showing lower values for plate temperatures and higher values for surface flux density or saturation current in T plasmas. The simulation results showed that the Be impurity flux to the divertor is higher in D plasmas, but Ni and Ne flux to the divertor are higher in T plasmas. Nevertheless, for the obtained T_e^{PLATE}, the W sputtering is dominated by Ni and Ne ions in T plasmas and Be in D plasmas.

3. The dimensional isotope identity experiment

The dimensional isotope identity experiment was performed in L-mode plasmas by running D (#100580) and T (#100134) discharges with matched engineering quantities such as magnetic field $B_t = 3.0$ T, plasma current $I_p = 2.5$ MA, NBI heating power with the two steps $P_{NBI} = 3.5$ MW and $P_{NBI} = 1.7$ MW, ohmic heating $P_{OH} = 1.5$ MW. For the D pulse, the deuterium concentration of 97% was measured. In the T pulse, the measured tritium concentration was 97 %. Similar to figure 1, the time evolution of the main plasma parameters for the dimensional isotope pair is presented in figure 13. The same vertical magnetic field configuration was used as in the case of the dimensionless isotope identity experiment (see figure 3). The higher NBI power level, indicated by the time interval at 13–14 s with the two vertical black lines in figure 13, was selected for time averaging. Deuterium plasma has more fast particles from NBI as the D beam yields more particles to obtain the same NBI power as the T beam. However, it is insufficient to make W_{dia} larger in D plasma because the thermal plasma confinement is about 10% higher in T plasma. That effect dominates in T plasma over the lower fast ion content. It is consistent with the detailed transport analysis of thermal particles, which extends beyond the scope of this work and will be addressed in a separate publication. The comparisons between kinetic

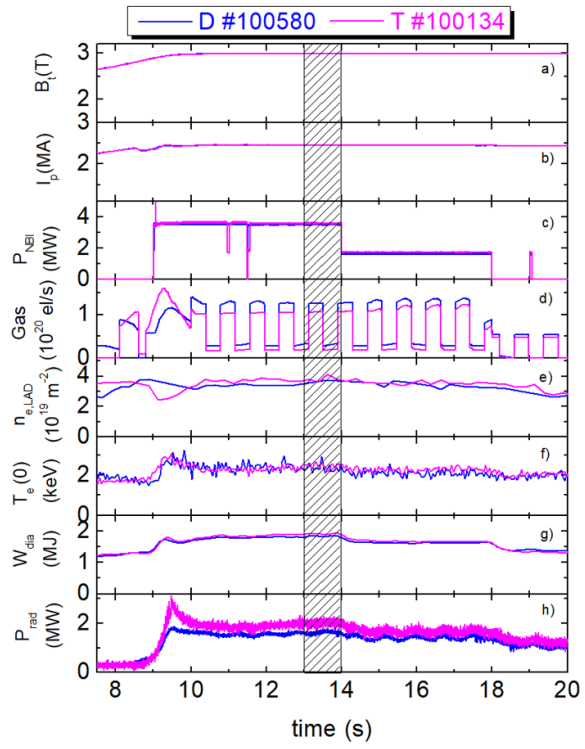

Figure 13. Time evolution of (*a*) the magnetic field B_t, (*b*) plasma current I_p, (*c*) the NBI heating power P_{NBI}, (*d*) major gas injection level, (*e*) the line average electron density n_{lad}, (*f*) the central electron temperature $T_e(0)$, (*g*) the diamagnetic energy W_{dia}, and (*h*) the total radiated power $P_{rad,}$ for D (blue, #100580) and T (magenta, #100134) discharges. The two vertical black bars indicate the time of interest in both pulses, at t = 13–14 s.

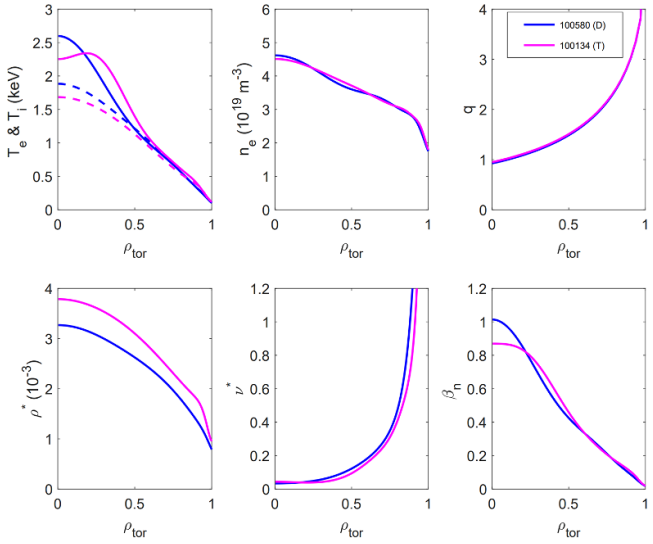

Figure 14. Comparison of the main dimensional (n_e, T_e, T_i) and dimensionless plasma profiles (ρ^*, ν^*, q, β_n) averaged in time between t = 13–14 s in D (#100580) and T (#100134) discharge as a function of the normalized radius.

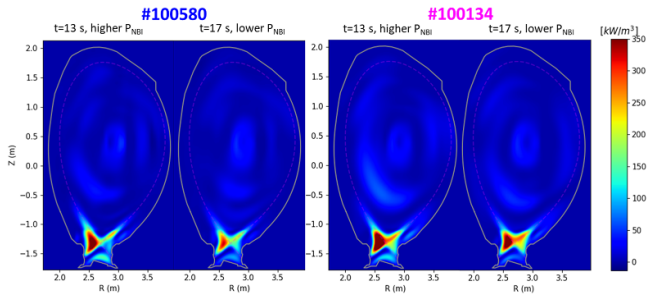

Figure 15. Tomographic reconstruction of the radiated power density in pulse #100580 for the D plasmas and in pulse #100134 for the T plasmas, for higher NBI power level at $t = 13$ s and lower NBI power level at $t = 17$ s, respectively.

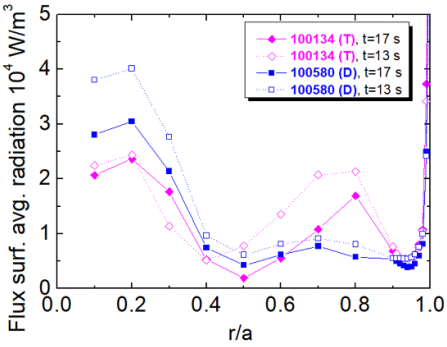

Figure 16. The flux-surface averaged profiles of the radiated density derived from the bolometry diagnostic as a function of the normalised radius for D (#100580) and T (#100134) discharge at t = 13 s and t = 17 s.

profiles T_e, T_i and n_e and the dimensionless quantities in D and T plasmas are illustrated in figure 14. Unlike in the case of the dimensionless identity pair, here, the n_e and T_e profiles in region $r/a > 0.5$ are similar for both isotopes. The bolometry reconstruction presented in figure 15 showed higher radiated power density in T plasmas in comparison to D plasmas. The flux-surface averaged profiles of the radiated power presented in figure 16, show higher values for T plasmas at normalized radius $0.6 < r/a > 0.9$, however in the central part at $r/a < 0.5$ the opposite trend was observed. This can be explained by different impurity transport and, as it is described later, different MHD instability behaviour in both discharges. The total radiated power (see figure 17(*a*)) as well as I_w (see figure 17(*b*)) and c_Ni (see figure 17(*c*)) are higher in T plasmas.

The divertor radiation presented in figure 17(*d*) is less sensitive to the NBI power and the difference between D and T is lower in comparison to P_{rad}. In contrary to the dimensionless isotope identity experiment, for which the influence of n_e on Be source was observed, in the dimensional isotope identity experiment for the same n_e, enhanced plasma–wall interaction (PWI) was observed in T plasmas. The production of neutral Be atoms in the main chamber depends on the isotope mass. The photon flux of Be II shown in figure 18, is larger in the T plasmas than in the D plasmas. It can be seen that the Be intensity is sensitive to gas puff modulation. The same oscillations are observed in the P_{rad}^{DIV} (see figure 17(*d*)). The radiated power, Be, W and Ni content depend on auxiliary heating and are higher for higher NBI power levels (see figure 17). In the divertor region closer to the separatrix, similar to the

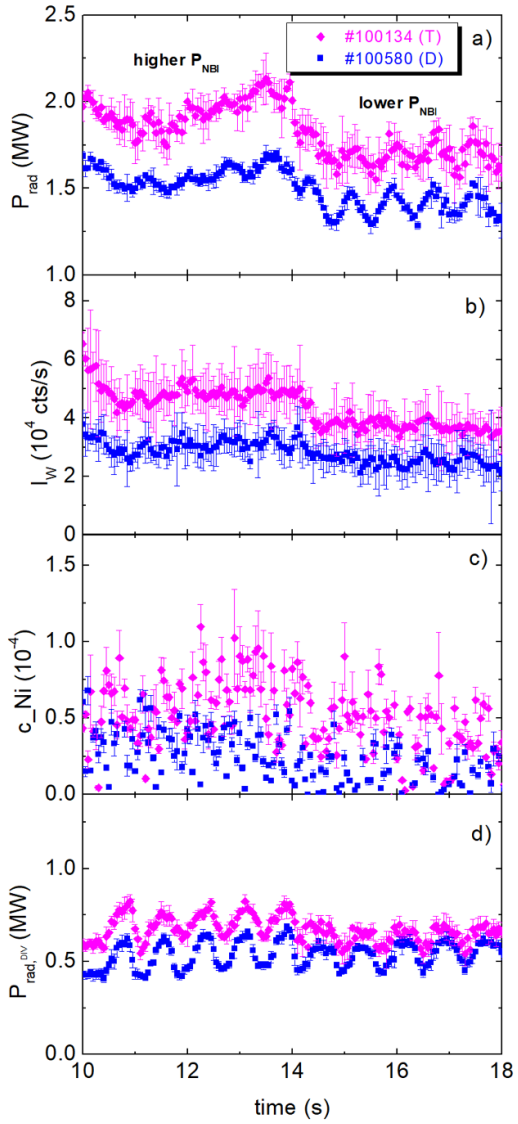

Figure 17. Time evolution of (*a*) the radiated power, (*b*) I_W, (*c*) cNi and (*d*) the divertor radiated power in the T pulse #100134 and the D pulse #100580 corresponding to two NBI power level steps.

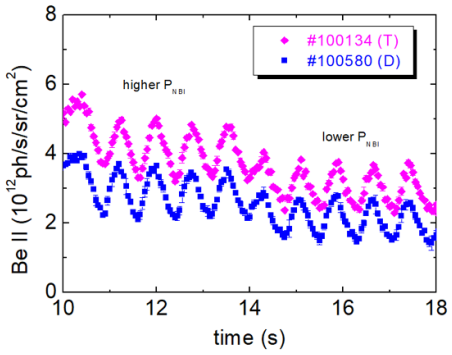

Figure 18. Time evolution of the photon flux of Be II line at 467 nm, measured at outer poloidal limiter in the T pulse #100134 and in the D pulse #100580 corresponding to two NBI power level steps.

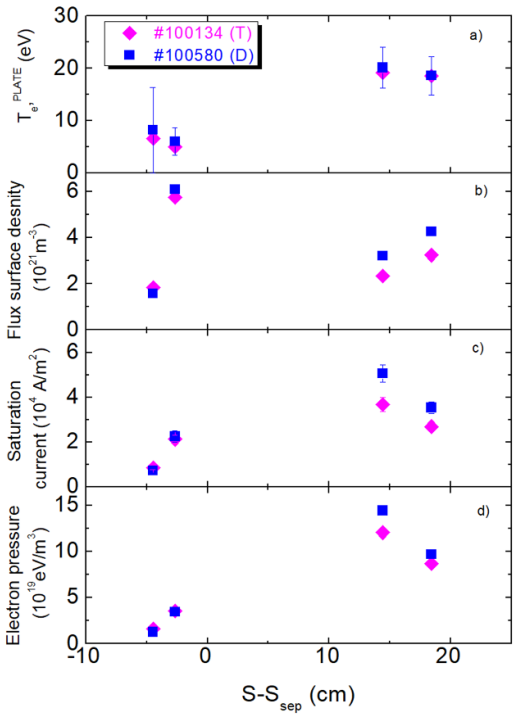

Figure 19. (*a*) The divertor plate electron temperature, (*b*) the surface flux density, (*c*) the saturation current and (*d*) the electron pressure measured by the Langmuir probes, as a function of distance along the vertical target from the separatrix for the T pulse #100134 and for the D pulse #100580 averaged over time 13–14 s.

plate electron temperature, the surface flux density, the saturation current and the electron pressure with the increased isotope mass were obtained (see figure 19). The discrepancies in the magnitudes of the parameters shown in figures 19(*b*)–(*d*) and 8(*b*)–(*d*), between the D and T plasmas can be attributed to variations in operational conditions, including plasma heating, density, and confinement. Additionally, differences in the physical properties of deuterium and tritium, such as their atomic masses and reaction rates, play a significant role in influencing the observed plasma behaviour. The plate temperature suggests that W sputtering in the divertor region is not related to T or D ions, but related to the Be and Ni. Due to stronger Be impurity flux to the divertor in T plasmas, the W sputtering by Be may be dominant in both D and T plasmas, similar to what was reported in [32].

The central impurity radiation is governed by the sawtooth (ST) cycle. Sawtooth oscillations change the behaviour of central plasma temperature and density profiles. Therefore, due to the correlation between a change in MHD activity and a change in impurity transport [25], the ST can be beneficial for impurity screening and for minimizing core impurity accumulation. This can be observed in the SXR signal presented in figure 20, which is registered by the horizontal soft x-ray cameras with the lines-of-sight presented in figure 3 (magenta line). Impurity emission increases monotonically between ST crashes, slowly levelling off towards the end of the cycle. It can be seen in figure 20(*a*) that T pulse #100134 is characterised by a slightly longer ST period (100–120 ms) in comparison to D pulse #100580 (80–100 ms). The differences in

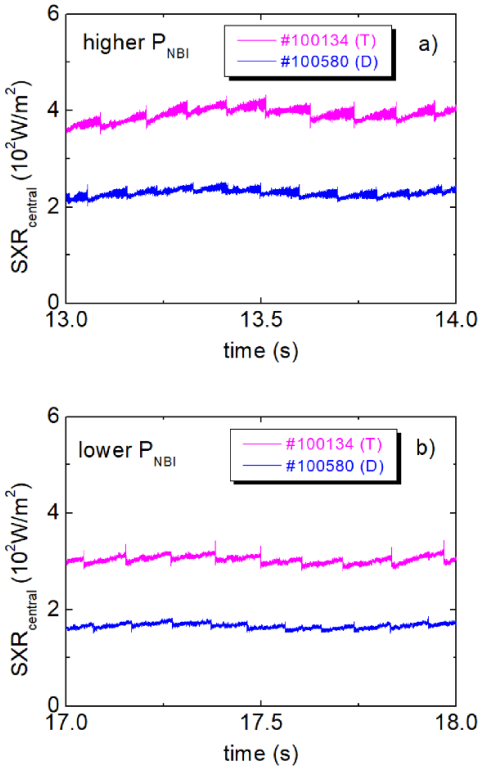

Figure 20. Soft-x-ray radiation from the central channel in the T pulse #100134 and in the D pulse #100580 for time intervals with (*a*) higher NBI power level and (*b*) lower NBI power level.

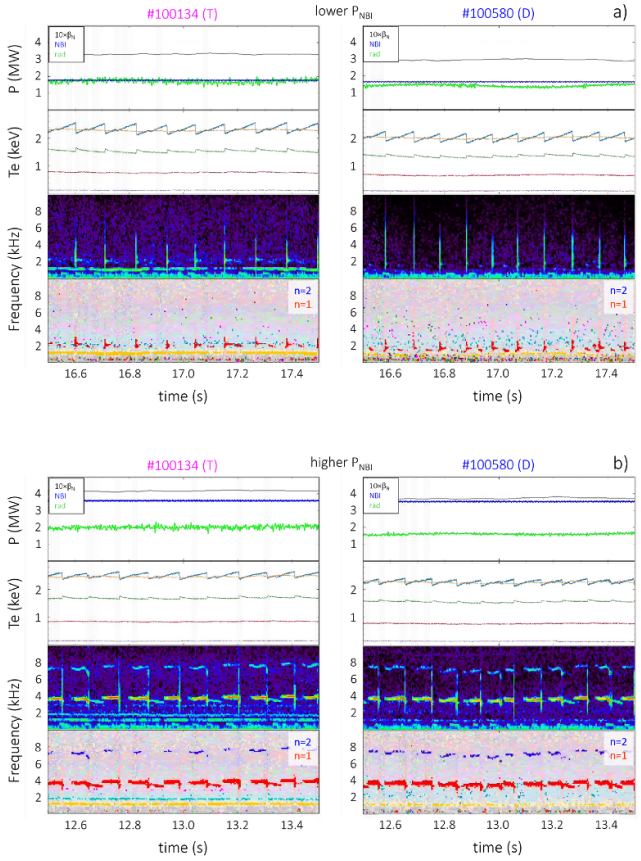

Figure 21. MHD analysis of the T pulse (left) and the D pulse (right). From top to bottom: total radiated power (green line), NBI power (blue line), electron temperature at different radii, spectrogram and toroidal mode number analysis from Mirnov coils.

radiated power density between D and T discharges, as shown in figures 5 and 16 for r/a < 0.3, can be partially attributed to ST instabilities, which influence impurity redistribution. Additional factors, including impurity source and transport, also contribute to the observed disparities. The characteristics of ST instabilities, such as period and amplitude, have dissimilar behaviours between dimensionless and dimensional experiments. In the dimensionless experiments, the ST period ranged from 70–80 ms for the deuterium (D) pulse #96092 (t = 17–18 s), and 90–110 ms for the tritium (T) pulse #100143 (t = 13–14 s). At very short periods, as in pulse #96092, the interval between each ST crash is relatively short. This means that the core plasma is continuously disrupted and quickly relaxed. This rapid cycling leads to frequent changes in the plasma's temperature and pressure profile and the rapid redistribution of heat and particles, which prevents impurities from settling or accumulating in the core, as they are continuously pushed outwards from the plasma core to the outer regions with each instability event. Conversely, when the ST period is longer, as in pulse #100143, the instability occurs less frequently. This allows impurities more time to accumulate in the core, as the plasma's internal dynamics enable them to remain there longer without being effectively expelled. The results suggest that there may be an optimum limit where the frequency can be sufficient to prevent excessive impurity accumulation. The same trend was observed for ST amplitude. The ST period and amplitude were notably higher in T plasmas in both experimental approaches. This is in agreement with models that predict the dependence of the ST period on the isotopic mass [36, 37]. The ST activity, and consequently the impurity behaviour, is also influenced by gas puff modulation. In D pulse #96092, the gas puff modulation occurs more frequently than in pulses #100143, #100134 and #100580 with similar modulation schemes (see figures 1 and 13). When the amount of gas puff decreases, ST suppression is observed, leading to a slightly longer ST period. Conversely, when the amount of gas puff increases, the ST period becomes shorter. This explains the variation in the ST period ranges across different pulses. A similar effect has been observed in other experiments at JET [38, 39]. Additional MHD analysis presented in figure 21 showed that for lower NBI power, in addition to the ST precursors and crashes, also a mild (1,1) mode is observed in #100134 and #100580, as highlighted by the n = 1 red component in the spectrogram between ST crashes (see figure 20(*a*)). For higher NBI power, additionally, the n = 2 harmonic (the blue component in figure 21(*b*) at frequency 8 kHz), develops for higher intensity of the inter-ST n = 1 mode. The internal 1/1 modes can influence transport or impurity behaviour. As presented in [40], the combination of helical core and plasma rotation augments the standard neoclassical inward pinch. However, these effects are observed mainly in hybrid operation scenario plasmas, without ST activity. In the analysed pulses the intensity of the 1/1 mode is very

low, without evident effect on the ST period or the shape of the electron temperature profiles. Thus, no relevant effect on transport or impurity behaviour is observed.

4. Conclusions

The dimensionless and dimensional Deuterium Tritium isotope identity experiments were performed at the JET Be/W wall in L-mode plasmas. A comparison of these two experimental approaches provides insight into whether isotope mass effects can explain the observed differences in impurity behaviours. Results for the low-Z, mid-Z and high-Z impurity behaviour under such conditions were reported in this paper. Both experiment types showed higher plasma radiation and increased Ni and W impurity content in T plasmas compared to D plasmas. This consistency suggests that isotope mass effects might contribute to enhanced impurity retention and radiation in T plasmas, with the heavier isotope possibly playing a significant role. In both dimensionless and dimensional experiments, Ni and W were identified as the main core radiators. The dimensionless experiments showed pronounced differences in impurity transport, with isotope mass effects likely contributing to the varying transport coefficients observed between D and T plasmas. This suggests that the mass of the isotopes affects how impurities behave within the plasma core. Diagnostic observations confirmed the presence of MHD instabilities, including ST. The characteristics of ST instabilities, such as period and amplitude, had dissimilar behaviours between dimensionless and dimensional experiments. Other MHD instabilities occurring in the plasmas were correlated with the NBI power level, which affected impurity behaviour. For higher P_{NBI} higher Be, Ni and W content was observed. In the dimensionless experiments, Be influx was higher in D plasmas due to lower electron density and stronger Be sputtering. The density difference necessary for creating the dimensionless match overshadowed the isotope mass effect on the Be source measured at the limiter. On the other hand, in the dimensional experiments, T plasmas exhibited a higher Be source, indicating a clear isotope mass effect, where the heavier T isotope leads to increased Be sputtering. This contrast highlights how isotope mass effects become more evident in the dimensional approach when comparing plasmas with similar n_{e}. The dimensionless experiments indicated that W sputtering in the divertor region was primarily driven by Ni in T plasmas and by Be in D plasmas, with minimal contribution from hydrogen isotopes. However, in the dimensional experiments, the Be impact on W sputtering was stronger in T plasmas, suggesting that isotope mass effects are more significant in the dimensional approach, particularly in influencing overall impurity interactions. Higher divertor plate temperatures, than those measured in both experiments, are needed for W sputtering by D or T. Results described in this paper experiments demonstrate that the impurity release can differ significantly depending on the hydrogen isotopes and the plasma properties. The comparison of dimensionless and dimensional isotope identity experiments indicates that isotope mass effects significantly influence impurity behaviour in D and T plasmas. These effects are more apparent in the dimensional approach, where mass-related differences in sputtering, transport, and impurity content become more pronounced, providing a deeper understanding of how different isotopes impact plasma properties.

Acknowledgments

This scientific paper has been published as part of the international project co-financed by the Polish Ministry of Science and Higher Education within the programme called ‘PMW’ for 2021-2024. This work has been carried out within the framework of the EUROfusion Consortium, funded by the European Union via the Euratom Research and Training Programme (Grant Agreement No 101052200—EUROfusion). Views and opinions expressed are however those of the author(s) only and do not necessarily reflect those of the European Union or the European Commission. Neither the European Union nor the European Commission can be held responsible for them. The views and opinions expressed herein do not necessarily reflect those of the ITER Organization.

ORCID iDs

A. Chomiczewska https://orcid.org/0000-0003-4931-728X
T. Tala https://orcid.org/0000-0002-6264-0797
W. Gromelski https://orcid.org/0000-0003-2683-8453
I. Ivanova-Stanik https://orcid.org/0000-0002-2766-8612
E. Kowalska-Strzęciwilk https://orcid.org/0000-0003-1710-9806
N. Wendler https://orcid.org/0000-0002-9765-6027
I.S. Carvalho https://orcid.org/0000-0002-2458-8377
G. Pucella https://orcid.org/0000-0002-9923-2770
A. Salmi https://orcid.org/0000-0002-3306-6335

References

[1] Cordey J.G. *et al* 1999 *Nucl. Fusion* **39** 301
[2] Saibene G. *et al* 1999 *Nucl. Fusion* **39** 1133
[3] Maggi C.F. *et al* 2019 *Nucl. Fusion* **59** 076028
[4] Weisen H. *et al* 2020 *J. Plasma Phys.* **86** 905860501
[5] Scott S. *et al* 1995 *Phys. Plasmas* **2** 2299
[6] Scott S. D. *et al* 1995 *Phys. Scr.* **51** 394
[7] Tala T. *et al* 2023 *Nucl. Fusion* **63** 112012
[8] Schneider P.A. *et al* 2023 *Nucl. Fusion* **63** 112010
[9] Frassinetti L. *et al* 2023 *Nucl. Fusion* **63** 112009
[10] Tanaka K., Okamura S., Minami T., Ida K., Mikkelsen D.R., Osakabe M., Yoshimura Y., Isobe M., Morita S. and Matsuoka K. 2016 *Plasma Phys. Control. Fusion* **58** 055011
[11] Ida K. *et al* 2019 *Nucl. Fusion* **59** 056029
[12] Guo W. *et al* 2019 *Nucl. Fusion* **59** 076012
[13] Chomiczewska A. *et al* 2024 *Nucl. Fusion* **64** 076058
[14] Telesca G. *et al* 2024 *Nucl. Fusion* **64** 066018
[15] Luce T.C., Petty C.C. and Cordey J.G. 2008 *Plasma Phys. Control. Fusion* **50** 043001
[16] Cordey J.G. *et al* 2000 *Plasma Phys. Control. Fusion* **42** A127
[17] Carvalho I.S. *et al* 2017 *Fusion Eng. Des.* **124** 841

[18] Vartanian S. *et al* 2021 *Fusion Eng. Des.* **170** 112511
[19] Huber A. *et al* 2007 *Fusion Eng. Des.* **82** 1327
[20] Fonck R.J., Ramsey A.T. and Yelle R.V. 1982 *Appl. Opt.* **21** 2115
[21] Lawson K.D., Coffey I.H., Rimini F. and Książek I. 2021 *Plasma Phys. Control. Fusion* **63** 105001
[22] Czarnecka A., Zastrow K.-D., Rzadkiewicz J., Coffey I.H., Lawson K.D. and O'Mullane M.G. 2011 *Plasma Phys. Control. Fusion* **53** 035009
[23] Sertoli M., Carvalho P.J., Giroud C. and Menmuir S. 2019 *J. Plasma Phys.* **85** 905850504
[24] Czarnecka A. *et al* 2019 *Plasma Phys. Control. Fusion* **61** 085004
[25] Putterich T. *et al* 2013 *Plasma Phys. Control. Fusion* **55** 124036
[26] Krawczyk N., Czarnecka A., Ivanova-Stanik I., Zagórski R., Challis C., Frigione D., Giroud C., Graves J., Mantsinen M.J. and Silburn S. 2018 *Rev. Sci. Instrum.* **89** 10D131
[27] Douai D. *et al 29th IAEA Fusion Energy Conf.* (*London, United Kingdom*, *16–21 October 2023*) (available at: https://media.superevent.com/documents/20230927/dd97c8b1d5d0c7459cd04098fde277d3/douai-ex-d.pdf)
[28] De Temmerman G. *et al* 2021 *Nucl. Mater. Energy* **27** 100994
[29] de la Cal E. *et al* 2022 *Nucl. Fusion* **62** 126021
[30] Brezinsek S. *et al* 2015 *Nucl. Fusion* **55** 063021
[31] Brezinsek S. *et al* 2019 *Nucl. Fusion* **59** 096035
[32] Brezinsek S. *et al* 2022 Gross erosion of tungsten in hydrogen, deuterium, tritium plasmas in JET equipped with beryllium first wall and tungsten divertor *25th Int. Conf. on Plasma Surface Interaction in Controlled Fusion Devices (PSI-25)* (*Jeju, South Korea, 12–17 June 2022*) (available at: https://users.euro-fusion.org/webapps/pinboard/EFDA-JET/conference/archived/2022/index.html#Document31136)
[33] Zagorski R., Ivanova-Stanik R.I. and Stankiewicz R. 2013 *Nucl. Fusion* **53** 073030
[34] Telesca G. *et al* 2021 *Nucl. Fusion* **61** 066027
[35] Mandrekas J. and Stacey W.M. 1995 *Nucl. Fusion* **35** 843
[36] Porcelli F., Boucher D. and Rosenbluth M.N. 1996 *Plasma Phys. Control. Fusion* **38** 2163
[37] Sauter O. *et al* 1999 Theory of Fusion Plasmas *Proc. Of the Joint Varenna–Lausanne Int. Workshop (Varenna, 1998)* ed J.W. Connor, E. Sindoni and J. Vaclavik (Editrice Compositori) p 403
[38] Nave M.F.F. *et al* 2001 *28th EPS Conf. on Controlled Fusion and Plasma Physics* (*Funchal, Portugal, ECA*, *18–22 June 2001*) vol 25A pp 961–4
[39] Koslowski R. *et al* 2001 *28th EPS Conf. on Controlled Fusion and Plasma Physics* (*Funchal, Portugal, ECA*, *18–22 June 2001*) vol 25A pp 965–8 (available at: https://info.fusion.ciemat.es/OCS/EPS2001/html/authors/nav/AutK04fr.html)
[40] Raghunathan M., Graves J.P., Nicolas T., Cooper W.A., Garbet X. and Pfefferlé D. 2017 *Plasma Phys. Control. Fusion* **58** 124002